JOURNAL OF SPACECRAFT AND ROCKETS
Vol. 30, No. 6, November–December 1993

Calculations and Comparisons of the Flowfield About an Ogive Cylinder at $M=3.5$

T. Hsieh,* F. J. Priolo,† and A. B. Wardlaw Jr.*
Naval Surface Warfare Center, Silver Spring, Maryland 20903

Laminar and turbulent Navier-Stokes and Euler calculations, with and without a separation model, were performed for a tangent-ogive cylinder. Comparisons were carried out between the predicted and measured surface pressures, and flowfield distributions of pitot pressure, static pressure, Mach number, and the total flow angle. The laminar solution was in overall best agreement with the experiment. However, an accurate turbulence transition model appears necessary to bring computations into close agreement with experiment.

I. Introduction

ABOVE an incidence of 5–10 deg, the flow of the leeside of a cylindrical body separates to form vortices. The interaction of this leeside vortical flow with control surfaces, such as fins and tails on missiles and aircraft, contributes to the highly nonlinear aerodynamics exhibited by these vehicles. Accordingly, prediction of such vortical flowfields is of practical importance. However, developing techniques for quantitatively describing vortical flow is difficult. Euler solutions cannot account for the formation of vortices, which arise from smooth body boundary-layer separation, without additional ad hoc modeling.[1,2] Limited wind-tunnel data are available and the generation of additional information is costly and time consuming.[3–5] The most promising approach appears to be the application of a Navier-Stokes solver. Recent progress in the development of Navier-Stokes (N-S) codes and supercomputers has made such an endeavor practical.

Numerous studies have demonstrated the applicability of Navier-Stokes codes to vortical flowfields.[6–12] However, few comparisons between calculations and experiment, particularly flowfield properties, have been published. The present work departs from these studies by selecting a sample case which has been studied extensively experimentally.[5] This facilitates comparison with experiment and sheds light on the accuracy of Navier-Stokes solutions combined with the available turbulence models. In addition, space-marching Euler solutions,[1] augmented with a separation model[2] are also presented.

Assessment of Navier-Stokes solutions requires a wide comparison of calculation and experiment, ideally involving flowfield information. Several such sets of experimental data are available[3–5]; however, only the study by Ragsdale[5] contains surface pressures and flowfield data. In the present work, computations are compared to this experimental example which features a tangent-ogive cylinder with a nose fineness of 4, cylinder diameter $D=3.0$ in., and total length of 7 calibers. This model was tested at Mach numbers 3.5 and 4, for incidence α between 0–15 deg. At the wall, T_w/T_{inf} was 3.4, where T_w is the wall temperature and T_{inf} is the freestream temperature. The freestream Reynolds number based on the model diameter is 3×10^6. The surface pressure was measured along 20 rays in the longitudinal direction and 23 circumferential planes. The flowfield was surveyed at an axial station 6.5 calibers from the nose. Measured flow properties were pitot pressure pp, static pressure p, Mach number M, and total flow angle $\epsilon=\tan^{-1}[(v^2+w^2)^{0.5}/u]$. The data for the 10- and 15-deg incidence cases at a freestream Mach number of 3.5 serve as the test examples for the current study.

II. Computational Schemes

A brief description of the numerical schemes and codes used in the present study is given in this section. The Courant-Fredricks-Lewy three-dimensional (CFL3D) code developed by Thomas et al.[9,13] is used to obtain the N-S solution. The governing equations are the single/double thin-layer approximations to the three-dimensional, time-dependent, compressible N-S equations, written in generalized coordinates (ξ, η, ζ) and conservation form as follows:

$$\frac{\partial}{\partial t}(Q)+\frac{\partial}{\partial \xi}(F)+\frac{\partial}{\partial \eta}(G-G_v)+\frac{\partial}{\partial \varsigma}(H-H_v)=0 \qquad (1)$$

where $Q=(J^{-1})(\rho, \rho u, \rho v, \rho w, e)^T$; F, G, H are the inviscid flux vectors; and the subscript v stands for the corresponding viscous flux vectors (see Ref. 9 for G_v and H_v); $J=\partial(\xi, \eta, \zeta)/\partial(x, y, z)$; ρ is the density; e is the total energy; and u, v, w are the x, y, z Cartesian velocity components. The equation of state for an ideal gas is used to define the pressure $p=(\gamma-1)[e-\rho(u^2+v^2+w^2)/2]$, where γ is the ratio of specific heats. Stokes' hypothesis for bulk viscosity and Sutherland's law for molecular viscosity are used to close the system. For turbulent flow calculation, the N-S equations are transformed to the Reynolds averaged equations by replacing the coefficients of molecular viscosity and thermal conductivity by the effective viscosity $\mu_e=\mu(1+\mu_t/\mu)$, where μ and μ_t are the molecular and turbulent viscosity, and the effective thermal conductivity $\kappa_e=(\mu c_p/Pr)[1+(\mu_t/\mu)(Pr/Pr_t)]$, where c_p is the specific heat at constant pressure. Pr and Pr_t are the molecular and turbulent Prandtl numbers. The turbulent viscosity is obtained from the work of Degani and Schiff[8] who modified the two-layer, algebraic eddy-viscosity model of Baldwin and Lomax.[14]

The computational algorithm used in CFL3D is outlined subsequently. The second-order-accurate flux-vector splitting scheme of Van Leer[15] is used for all of the generalized fluxes F, G, and H. For example, the flux difference in the ξ-direction at the ith cell is split into forward and backward contributions

$$\delta_\xi F=\delta_\xi^- F_i^+ + \delta_\xi^+ F_i^- = [F^+(Q^-)+F^-(Q^+)]_{i+1/2} - [F^+(Q^-)+F^-(Q^+)]_{i-1/2} \qquad (2)$$

The definitions of F^+ and F^- and the corresponding definition for Q^+ and Q^- can be found in Ref. 10. The diffusion terms are treated using a central difference whereas the linearized, backward-time approximation in delta form is used for the time differencing.

Presented as Paper 90-2853 at the AIAA 28th Atmospheric Flight Mechanics Conference, Portland, OR, Aug. 20–22, 1990; received Sept. 15, 1990; revision received Nov. 20, 1991; accepted for publication Dec. 10, 1992.

*Aerospace Engineer, Information and Mathematical Sciences Branch. Associate Fellow AIAA.

†Aerospace Engineer, Information and Mathematical Sciences Branch. Senior Member AIAA.

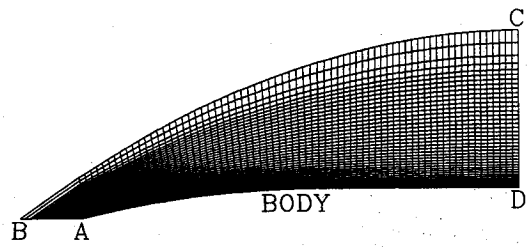

Fig. 1 Computational grid for ogive cylinder.

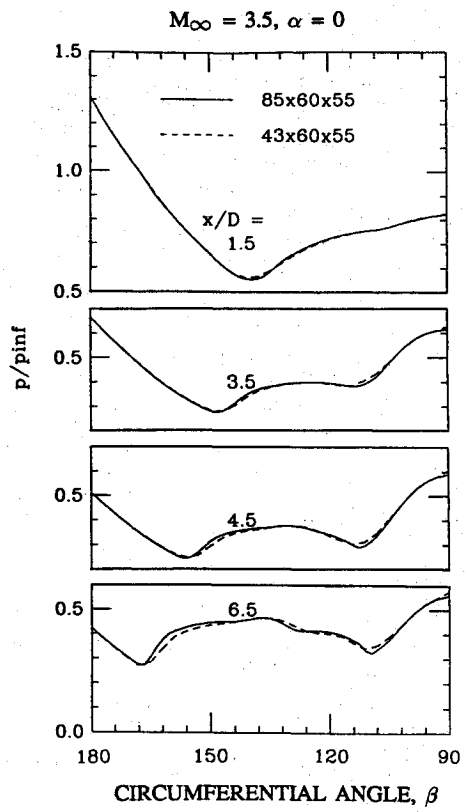

Fig. 2 Grid resolution.

When treated with the spatially factored scheme, the three-dimensional equations are solved by a series of sweeps through the three directions as follows:

$$\left[\frac{I}{J\Delta t}+\delta_\xi\left(\frac{\partial H}{\partial Q}-\frac{\partial H_v}{\partial Q}\right)\right]\Delta Q^* = -L(Q^n)$$

$$\left[\frac{I}{J\Delta t}+\delta_\eta\left(\frac{\partial G}{\partial Q}-\frac{\partial G_v}{\partial Q}\right)\right]\Delta Q^{**} = \left(\frac{I}{J\Delta t}\right)\Delta Q^* \qquad (3)$$

$$\left[\frac{I}{J\Delta t}+\delta_\xi\left(\frac{\partial F}{\partial Q}\right)\right]\Delta Q = \left(\frac{I}{J\Delta t}\right)\Delta Q^{**}$$

$$Q^{n+1} = Q^n + \Delta Q$$

where $-L(Q^n)$ is the discrete representation of the spatial-derivative terms in Eq. (1) evaluated at time level n. The algorithm is written in delta form so that the steady-state solution is independent of the time step Δt. The implicit spatial derivatives for the convective and pressure terms are first-order accurate. This leads to a block tridiagonal solution. Second-order-accurate upwind-biased spatial differencing is maintained for the residual calculation producing a second-order steady-state solution.

The computational domain for the ogive-cylinder calculation is shown in Fig. 1, where AD is the body surface, AB the singular axis, BC the far-field inflow boundary, and CD the outflow plane. Boundary conditions are explicitly implemented. On the body surface, no-slip, no-penetration, and isothermal wall conditions are imposed. For the singular axis, a continuation of cell-center flow variables is imposed. At the far-field inflow boundary, the freestream condition holds. At the outflow plane, an extrapolation of flow quantities is implemented. The flow is assumed to be symmetrical with respect to the pitch plane, so only half of the cross-flow plane needs to be computed. The initial conditions are the uniform freestream conditions everywhere with $u=v=w=0$ on the solid boundary.

A space-marching Euler solver called ZEUS[1,2] is also used in the present study. The ZEUS code numerically solves the inviscid shock layer for tactical missiles in supersonic flight by spatial marching. ZEUS combines a multiple-zone gridding technique with a second-order extension of Godunov's method[16] to integrate Euler's equations. The Godunov method is an upwind scheme based on solving the Riemann problem for steady supersonic flow. The method is cast in control volume form and consists of a predictor and corrector step. The predictor step advances the primitive variables using Euler's equations in nonconservation form. The corrector step modifies Godunov's method by assuming linear property variations within each control volume. Property derivatives are computed using a limited central differencing procedure. The separation model described in Ref. 2 has been incorporated into ZEUS to simulate boundary-layer separation on the leeside of the body.

III. Results and Discussion

The CFL3D code was implemented on a minisupercomputer (Alliant FX-80) and all of the computational results reported in this paper were completed on this machine. The CPU time required to run the code was 0.002 s/time step/grid point and each run generally required 1500 time steps to reach steady state. The three-dimensional grid was generated by rotating the grid depicted in Fig. 1 about the missile axis. Grid sizes in the circumferential j, radial k, and axial i directions were 43×48×72 and 43×52×71 for laminar and turbulent calculations, respectively, resulting in a run time of approximately 132 h for a turbulent case. A uniform distribution of grid points was used in the i direction. In the j direction, a constant grid spacing of 3 deg was used between the lee-

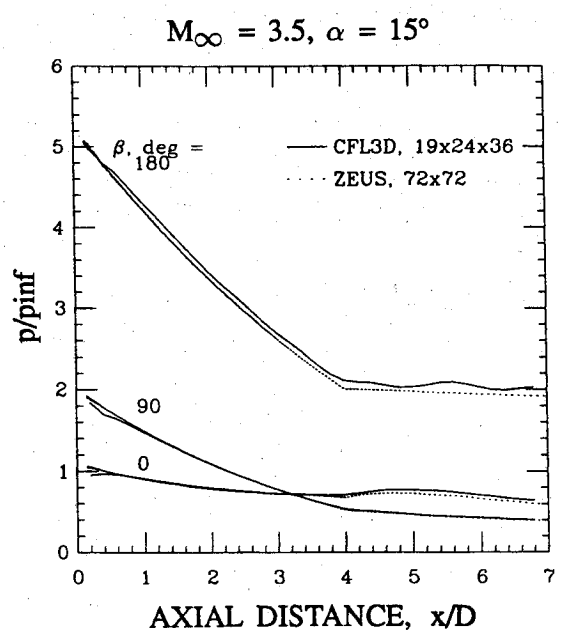

Fig. 3 Comparison of longitudinal pressure distribution of inviscid solutions.

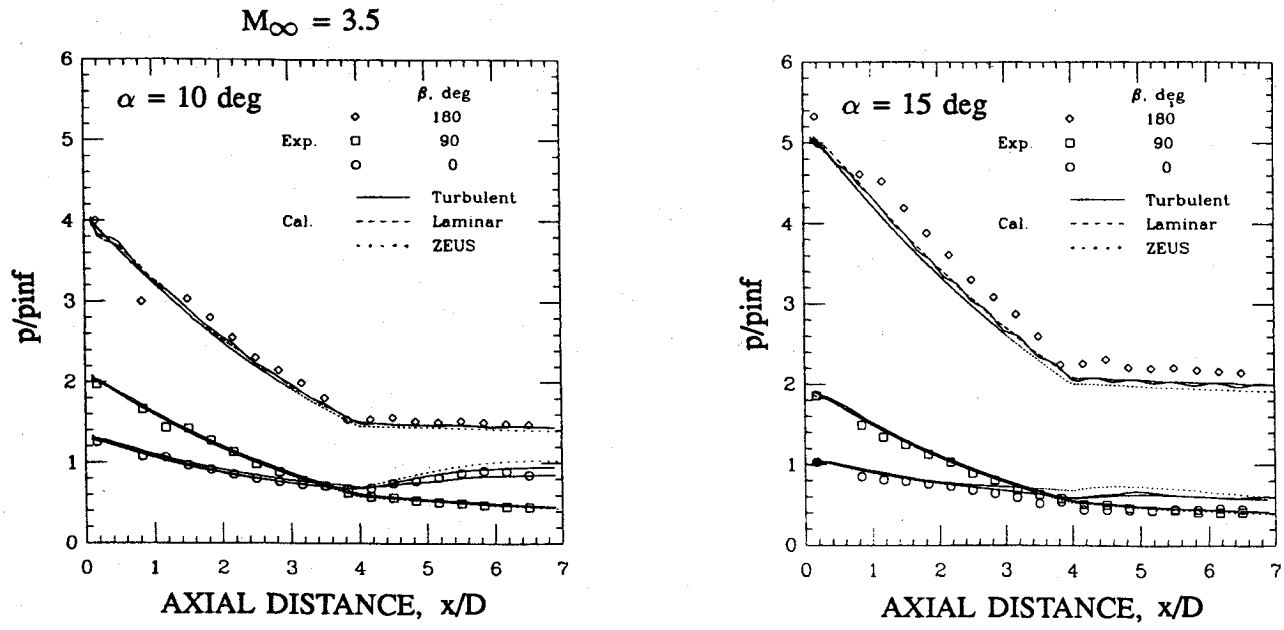

Fig. 4 Comparison of longitudinal surface pressure between experiment and solutions.

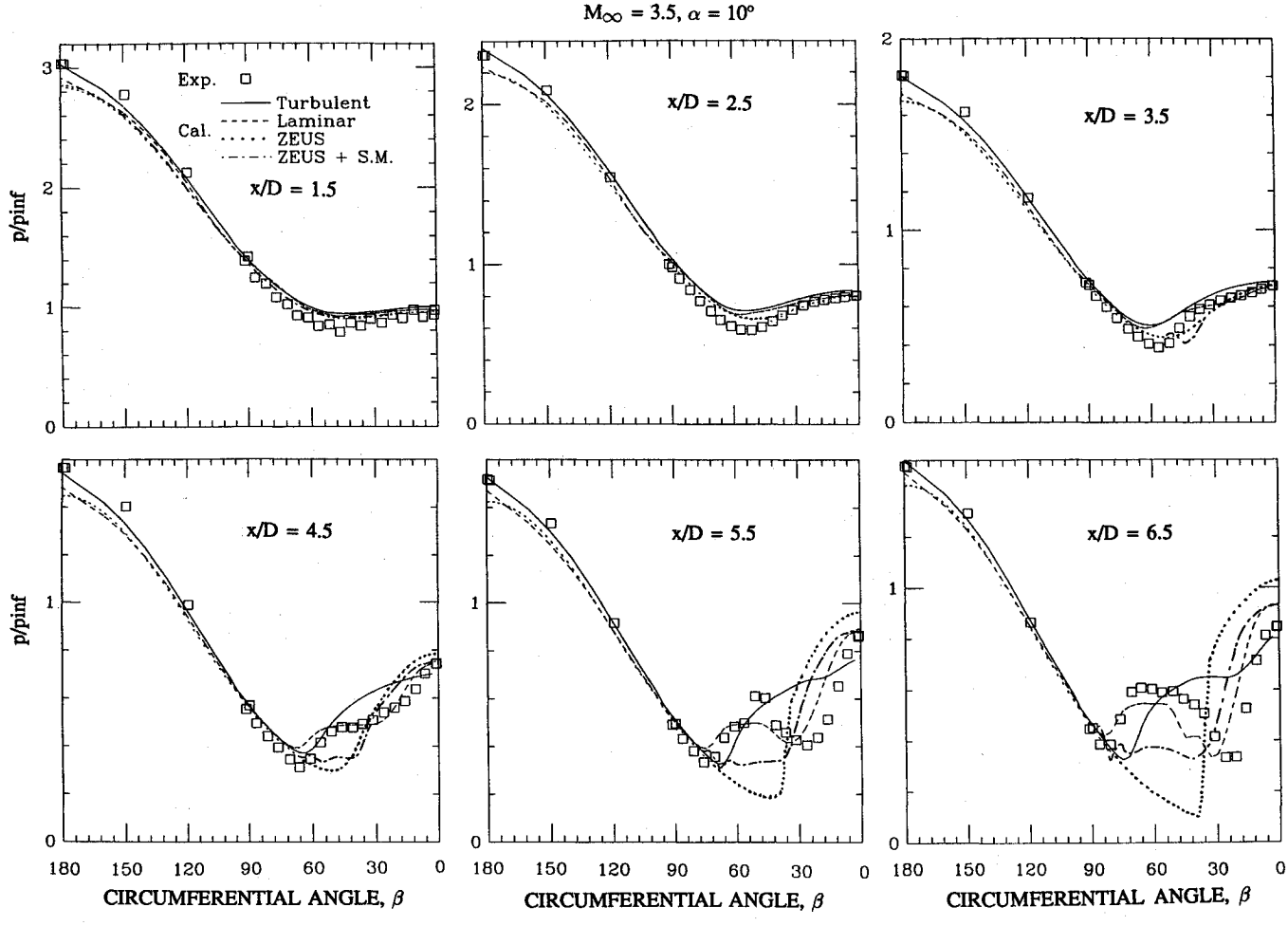

Fig. 5 Comparison of crossflow surface pressure between experiment and solutions, α=10 deg.

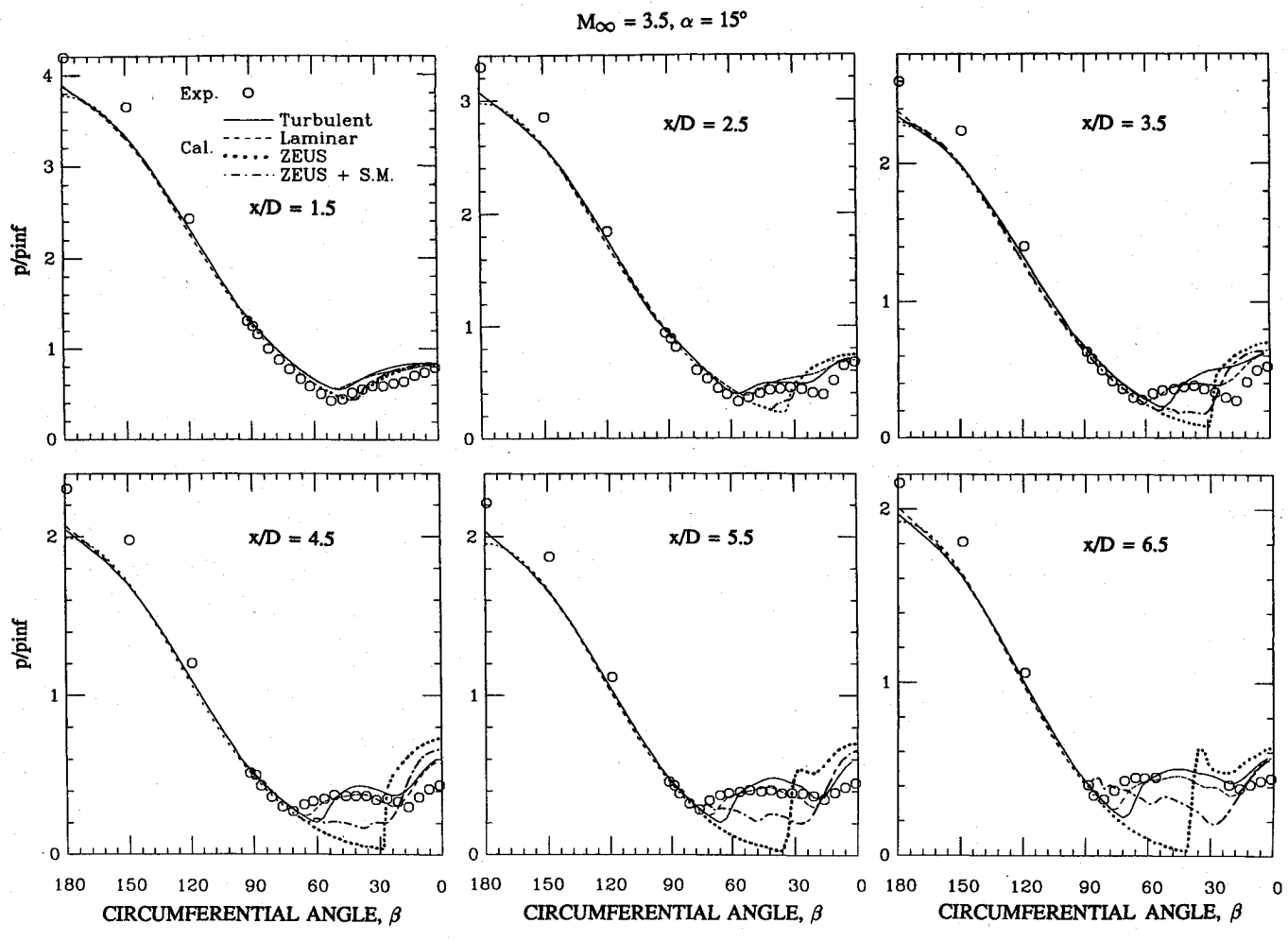

Fig. 6 Comparison of crossflow surface pressure between experiment and solutions, α=15 deg.

ward plane, β=0 and 99 deg, followed by a smooth increase to 10 deg at β=120 deg. The circumferential grid spacing remained constant from this point to the windward side, β=180. The laminar and turbulent grids differed in the point distribution in the k direction. A stretching function $f(k)$, where $0 \le f \le 1$, was used to define points in the radial direction according to:

$$S(k)/D = f(k)\, S_{\max}/D$$

Here S is the radial distance measured from the body surface to point k, and f was selected to concentrate grid points near the body surface. The distance between the wall and the first point on the turbulent grid was about two orders of magnitude smaller than on the laminar one, i.e., $f(2)=0.001$ for the laminar grid and $f(2)=0.00003$ for the turbulent grid, insuring at least two points within the laminar sublayer. The additional points for the turbulent grid were added near the wall resulting in the boundary-layer transverse coordinate for the law of the wall, $y_2^+ < 1.0$ and $y_3^+ < 5.0$. The $f(k)$ distributions for $f > 0.001$ were very similar for both laminar and turbulent grids insuring the same resolution in both cases.

The sensitivity of the solution to outer boundary location was studied by increasing the radial extent of the basic grid shown in Fig. 1 by 40%. The solution obtained for this domain using a 43×60×55 grid was nearly identical to that on the basic grid. The influence of grid size on the solution was examined by doubling the number of points in the circumferential direction. As is shown in Fig. 2, only a slight difference in surface pressure was noted at $x/D=6.5$. These tests suggested that the basic grid, shown in Fig. 1, was adequate for this problem, and all of the results reported in this paper were obtained using it.

To insure that the CFL3D code was implemented correctly, Fig. 3 compares inviscid surface pressures obtained with this code and the ZEUS space-marching Euler code at Mach=3.5, α=15 deg on planes of β=0, 90, and 180 deg. Slight differences were found on the leeward and windward planes, otherwise the results were very consistent. The slight waviness in the computed axial pressure shown in Figs. 3 and 4 with the CFL3D code may be attributed to the relatively small number of axial grid points.

In the following subsections, laminar CFL3D, turbulent CFL3D, and ZEUS surface and flowfield pressures are compared to experimental measurements at Mach 3.5. Surface pressures span the entire body while the flowfield information is at $x/D=6.5$. ZEUS calculations were performed with and without the separation model.

Axial Pressure Distribution

The comparisons of axial surface pressure at β=0, 90, and 180 deg at α=10 and 15 deg are shown in Fig. 4. At α=10 deg, the experiment and calculations are in close agreement. Slight differences are visible on the leeward side near the aft end with the inviscid solution predicting higher pressure. At α=15 deg, significant differences are present between all solutions and the data. On the windward side, the experimental values are consistently higher than calculations. However, the solutions obtained by the two codes are in close agreement. The same situation has been reported in Ref. 12. This discrepancy may be attributable to two sources of experimental error: 1) deflection of the model support system during the test which increases the angle of attack and 2) pressure-tap hole-size errors which increase the measured pressure. On the leeward side, the solutions are seen to give higher pressures than the

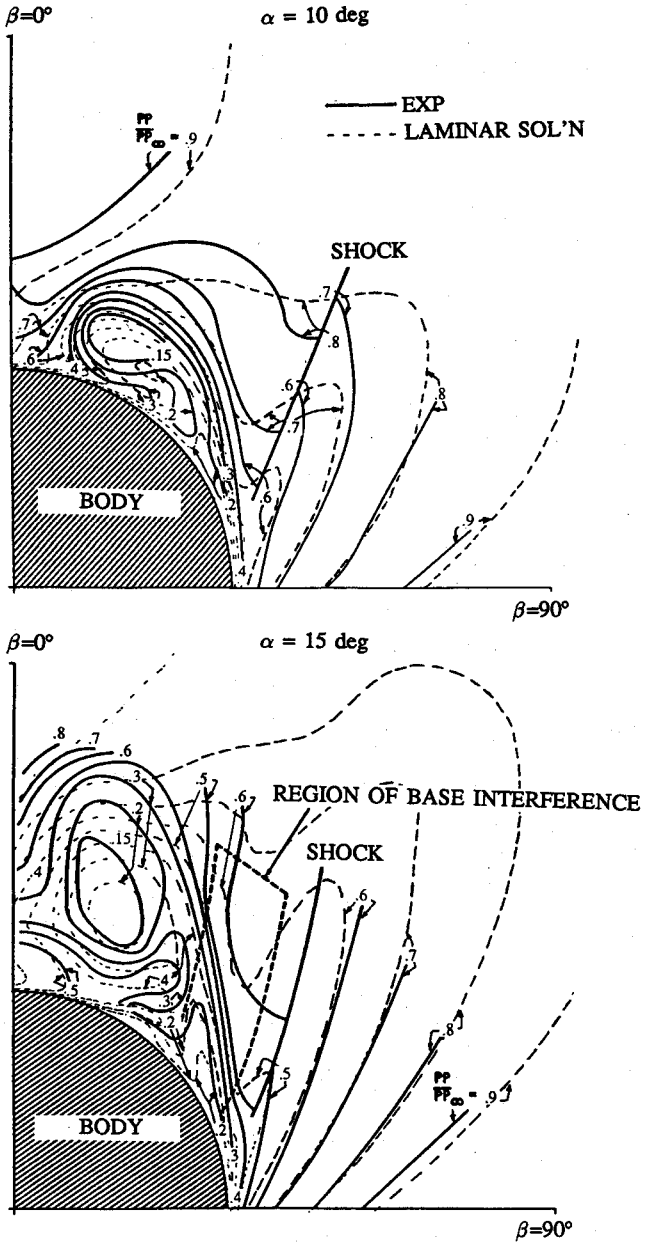

Fig. 7 Comparison of pitot pressure contour between experiment (solid line) and laminar solutions (broken line), $x/D=6.5$.

measured values for $x/D>3$. Here again the inviscid solution exhibits the largest discrepancy.

Crossflow Surface Pressure

Figures 5 and 6 present comparisons of computed and measured circumferential pressure distributions at six stations for $\alpha=10$ and 15 deg. Laminar, turbulent, inviscid, and inviscid plus separation model predictions are illustrated. On the windward side at $\alpha=10$ deg (Fig. 5), experimental and all computational results are in good agreement. Crossflow separation first occurs at $x/D=3.5$, and at stations forward of this point the viscous solutions overpredict the pressure slightly on the leeside ($0<\beta<90$ deg). Downstream of the station at which separation occurs there are significant discrepancies among the calculations and between the calculations and experiment. The inviscid flow solution predicts a strong crossflow pressure gradient/shock which differs most with the experimental data. Adding the separation model to the inviscid solution improves the agreement to some extent, but the plateau leeward of the separation point is too low. The laminar solution agrees best with the general trend of the experimental data but somewhat underpredicts this plateau at $x/D=5.5$ and 6.5. The predicted laminar crossflow separation location is slightly ahead (windward side) of the measured point as shown in Fig. 5. The turbulent solution, as expected, features a leeward displacement of the crossflow separation point relative to the laminar solution. Here, the experimental separation location (taken to coincide with the minimum pressure location) lies between the laminar and the turbulent one. In addition, the second pressure minimum exhibited by experiment near $\beta=30$ deg is absent from the turbulent solution.

On the windward side at $\alpha=15$ deg (Fig. 6), all computed pressures, which are in close agreement, underpredict the experiment. The agreement between computation and experiment improves as β decreases. Crossflow separation and thus vortex formation at $\alpha=15$ deg occurs farther forward at $x/D=2.5$. At $x/D=2.5$ and 3.5 the laminar solution and experiment are in close agreement except on the leeside for $\beta<30$ deg. Unlike the case of $\alpha=10$ deg, at $x/D=4.5$, 5.5, and 6.5, the experimental separation point occurs ahead of the laminar one. Consequently, the discrepancy between the turbulent separation point and measurement is larger. In the experiment,[5] base interference was noted at $\alpha=15$ deg and this may have caused the boundary layer near $\beta=60$ deg to thicken (see Fig. 7), which in turn forced the experimental separation point windward. Possibly this accounts for the discrepancy between calculation and experiment. Nevertheless, the measured and laminar prediction of the pressure plateau are in close agreement, and the turbulent solution follows the same trend. Based on the preceding comparisons of surface pressure, the laminar solution is again seen to best agree with experiment. In the following subsections, comparisons will be made for the flow quantities in the crossflow plane at $x/D=6.5$ using the laminar solution unless otherwise stated.

Pitot Pressure Contour

Figure 7 presents comparisons of pitot pressure contours for $\alpha=10$ and 15 deg. The solid lines are the experimental data and the broken lines are the laminar solution. Clearly the measured vortex is somewhat farther away from the body than the computed one, particularly for the 10-deg incidence case. At $\alpha=15$ deg, the computed contours above the vortex core differ significantly from the experiment. This may be due to the effect of base interference, indicated by the rectangular region in Fig. 7, which pushes the vortex to the upper left. At both incidences, the minimum computed pitot pressure contour in the vortex core is 0.2 which is higher than the experimental value of 0.15. The crossflow shock is smeared in the computation but the location is very close to the measured one. Contours ahead of the crossflow shock agree very well with the experiment.

A comparison between computed and measured pitot pressure is made along the radial distance S at constant β lines in Fig. 8. Here, the symbols represent the experiment, the solid lines are the laminar solution, and the broken lines are the turbulent solution. For both incidences, the agreement between experiment and computations is excellent for $\beta=180$, 90, 76, and 60 deg. On the leeside, for $0<\beta<45$ deg, this good agreement deteriorates, particularly at $\alpha=15$ deg. At $\alpha=10$ deg incidence and $\beta=45$ and 30 deg, the turbulent and laminar solutions miss the s-shape profile shown by the experiment. At $\beta=15$ and 0 deg, the turbulent and laminar solutions exhibit a comparable error. The difference between laminar and turbulent solutions at $\alpha=15$ deg is small, but both solutions differ significantly with the experimental data. The influence of base interference on the experimental data remains an open question.

The pitot pressure comparison suggests that the laminar solution is in better overall agreement with the experiment. Obviously, with a Reynolds number based on cylinder diameter of 3×10^6, it is unlikely that the flow will remain laminar over the entire body. The experiment likely features a significant laminar region upstream of the separation line. This type of mixed laminar and turbulent flow has been reported in Ref. 17. To correctly simulate the mixed laminar and turbulent flow over the body, a new turbulence model capable of handling transitional flow must be developed. This observation is strongly supported by the results at $\alpha=10$ deg. In

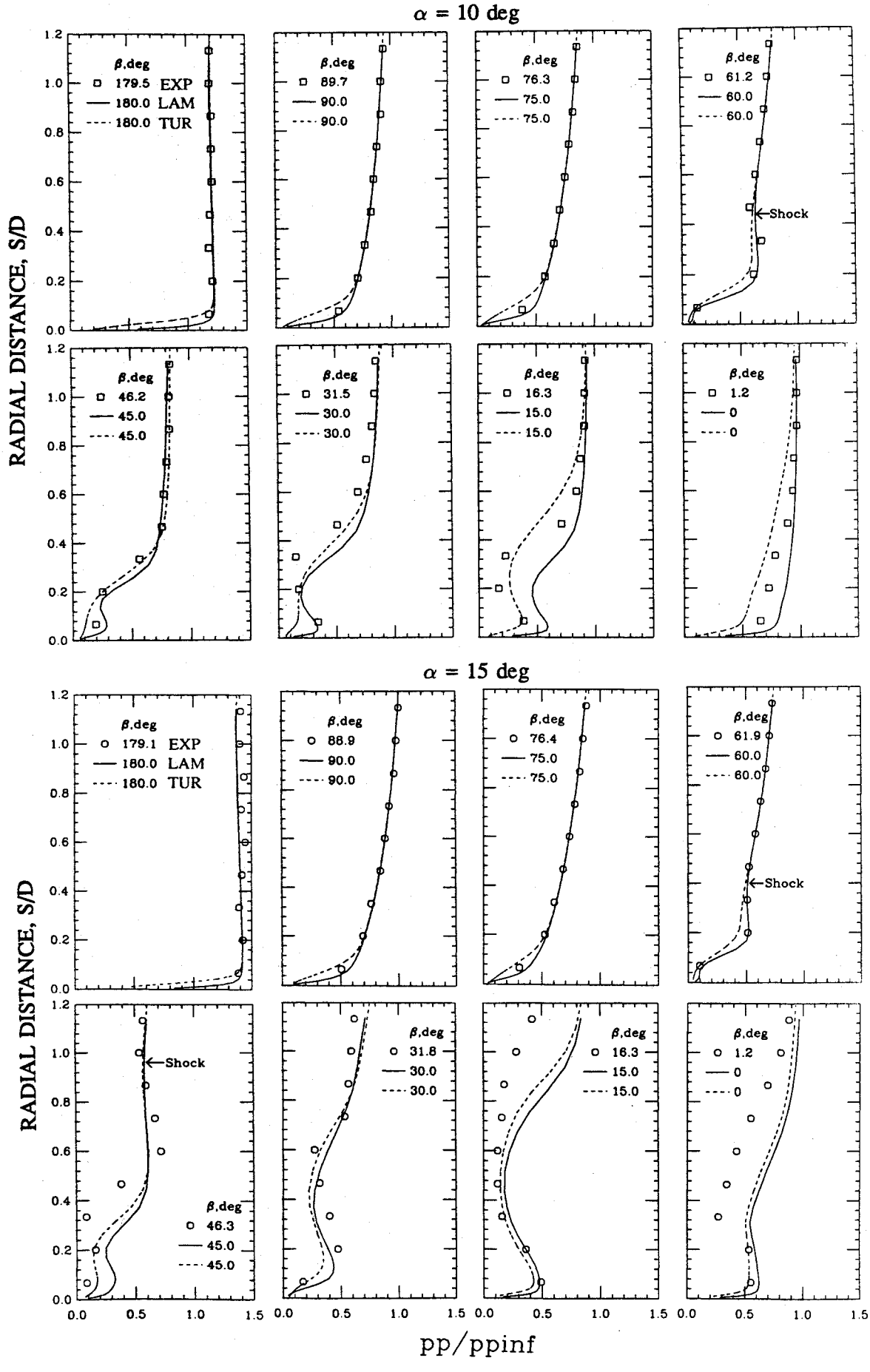

Fig. 8 Comparison of pitot pressure along radial direction at various circumferential angles, experiment (symbols), laminar (solid line), and turbulent (broken line) solutions, $x/D=6.5$.

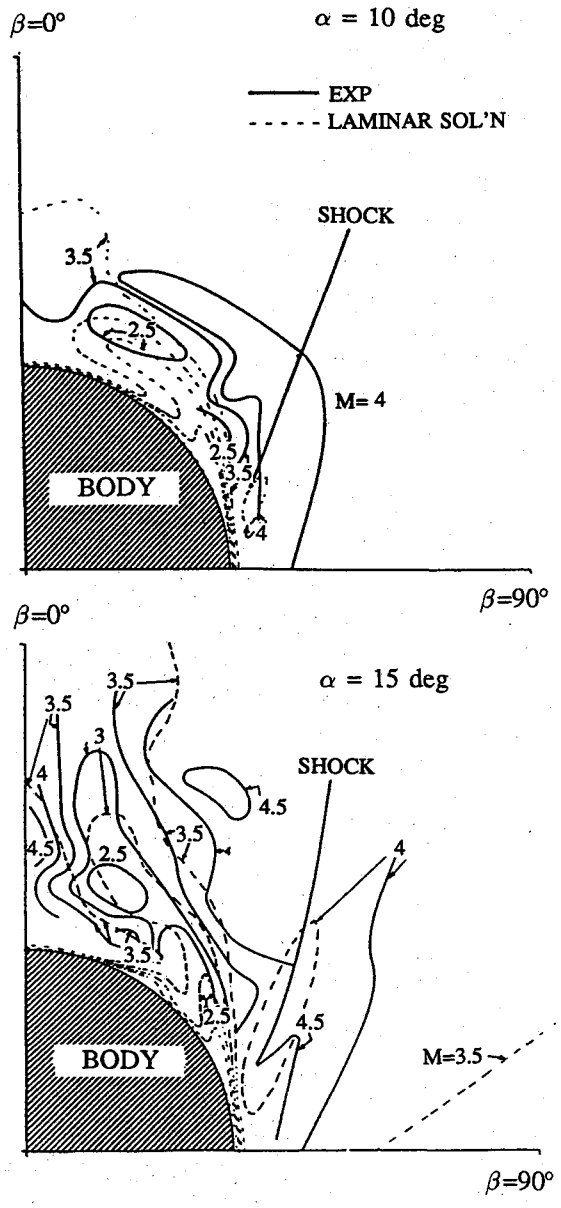

Fig. 9 Comparison of Mach contours between experiment (solid line) and laminar solutions (broken line), x/D=6.5.

addition, one would not expect the simple algebraic-turbulence model used in the calculation to suffice for this complex vortical flowfield.

Mach Contour

Comparisons between experiment and laminar predictions of Mach contours for α=10 and 15 deg are shown in Fig. 9. For 10-deg incidence, the computed Mach 4 contour covers a much smaller area than the measured one. Large differences also occur near the pitch plane for Mach 3.5. For 15-deg incidence, the computed Mach number never reaches 4.5 whereas the experimental data show two such areas. Also the computed Mach 4 contour covers a smaller area than the measured one. Near the vortex center, the computed Mach number never reaches the 2.5 value recorded in the experiment. Among all of the compared flowfield variables, the discrepancies between computed and measured Mach number contours are the largest.

Total Flow Angle Contour

Comparisons between experiment and laminar predictions of total flow angle contours for 10- and 15-deg incidences are shown in Fig. 10. The agreement is fairly good, but the measured total flow angles are generally higher, exceeding the computed values by 6–10 deg in some areas. The computed maximum total flow angle occurs in the vicinity of the primary flow separation location (β=75–90 deg) near the body and the measured one appears above the body near β=60.

Velocity Vector

Comparisons between the experiment and the laminar predictions of the crossflow velocity vectors are shown in Fig. 11. The length of the velocity vector is proportional to velocity magnitude for the computed results only. Unlike the pressure contour plots, it is difficult to detect the difference between the measured and calculated vortex core location. A detailed velocity vector plot for 15-deg incidence is shown in Fig. 12. The secondary crossflow separation location S_2 and the resulting secondary vortex V_2 are visible in this figure. The experiment did not have sufficient resolution close to the body to detect these structures. The positions of the primary and secondary vortices are β=17 deg, S/D=0.235 and β=38 deg, S/D=0.018 and the locations of the primary and secondary separation points are β=7 and 30 deg, respectively. Similarly, at 10-deg incidence, the primary vortex is located at β=26

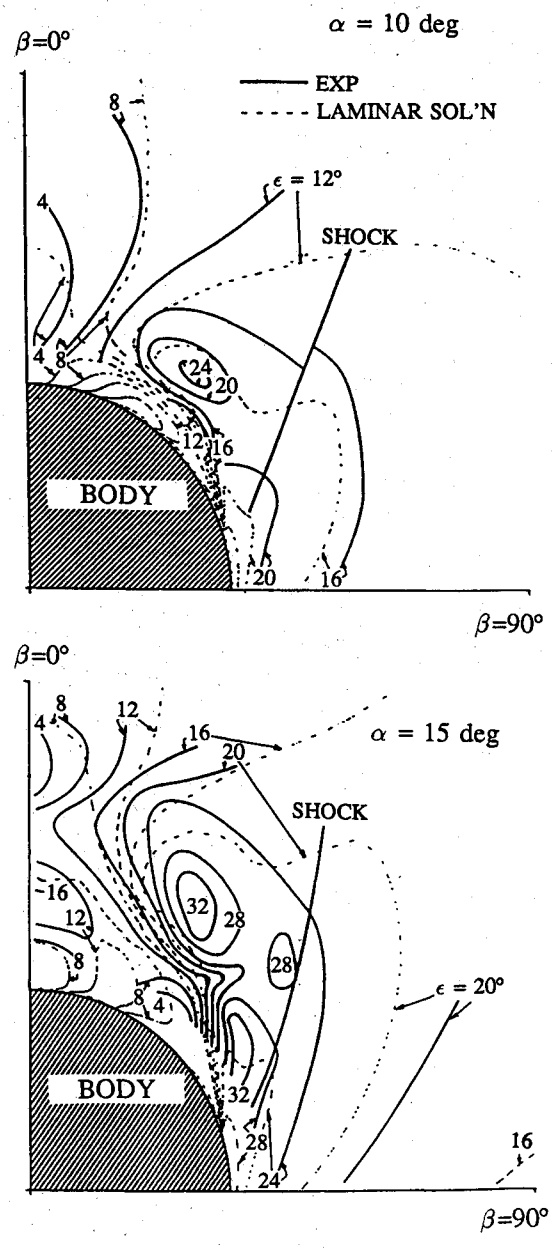

Fig. 10 Comparison of total flow angle contours between experiment (solid line) and laminar solutions (broken line), x/D=6.5.

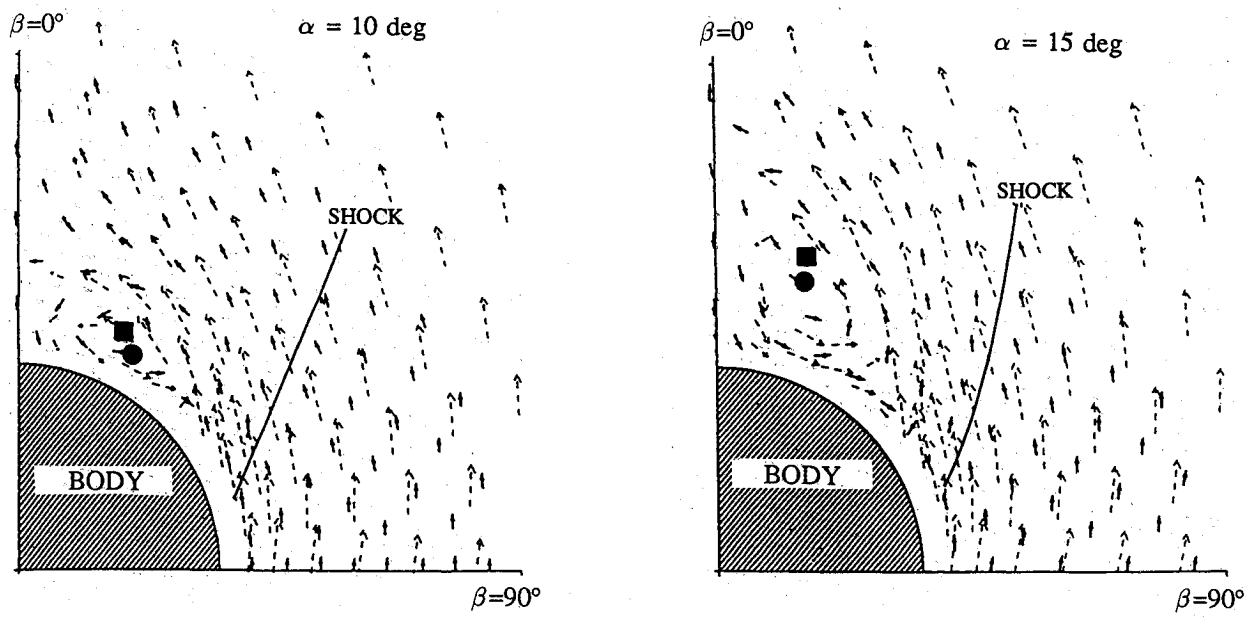

Fig. 11 Comparison of velocity vectors between experiment (solid line) and laminar solutions (broken line), $x/D=6.5$; estimated vortex center experiment (square) and laminar solution (circle).

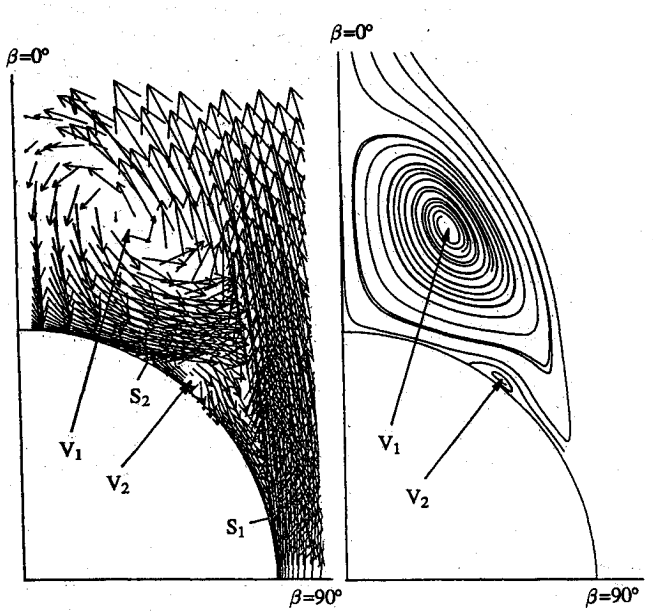

Fig. 12 Detailed plot of crossflow velocity vectors and streamlines for laminar solution, $x/D=6.5$, $\alpha=15$ deg.

deg, $S/D=0.078$, whereas the primary separation point is positioned at $\beta=74$ deg. An enlarged velocity vector plot of the laminar solution (not shown) suggests that the secondary vortex is located at $\beta=50$ deg, $S/D=0.008$.

IV. Summary

Calculations have been carried out using the CFL3D Navier-Stokes and ZEUS Euler solvers. Navier-Stokes computations were performed assuming laminar and turbulent flows whereas the Euler results were obtained with and without a separation model. Calculations were completed for a tangent-ogive model which had been tested at Mach 3.5 and incidences of 10 and 15 deg. Thorough comparisons were performed among the numerical solutions and between computation and experimental data. This consisted of examining surface pressures over the body, and pitot pressure, static pressure, Mach number, and the total flow angle contours on a crossflow plane at $x/D=6.5$. The following observations can be drawn from the present investigation.

1) Inviscid computations do not predict the correct flowfield structure. Augmenting the inviscid solver with a separation model produces the correct qualitative description of the flowfield.

2) The laminar solution gives the overall best agreement with experiment for this particular case. Application of Degani and Schiff's modified Baldwin-Lomax turbulence model increases the discrepancy between calculation and experiment at 10- and 15-deg incidences.

3) Surface pressure predictions on the windward plane at 15-deg incidence were in close agreement with one another, but are consistently lower than experiment. Deflection of the model during testing is a possible cause of this discrepancy.

4) Pitot pressure and Mach number are the flowfield variables which were most and least accurately predicted, respectively. At 15-deg incidence, the base interference may have affected the accuracy of the data on the leeside.

5) Comparison between calculations and experiment suggests the occurence of transitional flow over the test model. This emphasizes the necessity of developing turbulence models capable of handling transitional flow.

To facilitate future code development and verification, accurate measurements of pitot pressure, velocity components and their fluctuating quantities, and skin friction would be very helpful in evaluating numerical algorithms, turbulence models, and location of crossflow separations. As is well known, these data are very expensive to obtain, but the utility of such results is appropriately large.

References

[1]Wardlaw, A. B., Jr., and Priolo, F. J., "Applying the ZEUS Code," Naval Surface Warfare Center, NSWC TR 86-508, Silver Spring, MD, Dec. 1986.

[2]Priolo, F. J., and Wardlaw, A. B., Jr., "Euler-Space Marching Computations with Crossflow Separation for Missile-Type Bodies," AIAA Paper 90-0616, Jan. 1990.

[3]Jorgensen, L. H., and Perkins, E. W., "Investigations of Some Wake Vortex Characteristics of an Inclined Ogive-Cylinder Body at Mach Number 2," NACA 1371, May 1955.

[4]Thomson, K. D., and Morrison, D. F., "The Spacing, Position, and Strength of Vortices in the Wake of Slender Cylindrical Bodies at Large Incidence," *Journal of Fluid Mechanics*, Vol. 50, Pt. 4, 1971, pp. 751–783.

[5]Ragsdale, W. C., "Flow Field Measurement Around an Ogive-Cylinder at Angle of Attack up to 15 Degrees for Mach Number of 3.5 and 4.0,"

Naval Ordnance Lab. TR 72-198, Silver Spring, MD, Aug. 1972.

[6]Hsieh, T., "Calculation of Viscous, Sonic Flow Over Hemisphere-Cylinder at 19 Degree Incidence: The Capturing of Nose Vortices," AIAA Paper 81-0189, Jan. 1981.

[7]Hankey, W. L., Graham, J. E., and Shang, J. S., "Navier-Stokes Solution of a Slender Body of Revolution at Incidence," *AIAA Journal*, Vol. 20, No. 6, 1982, pp. 776–781.

[8]Pulliam, T. H., and Steger, J. L., "Recent Improvements in Efficiency, Accuracy, and Convergence for Implicit Approximate Factorization Algorithms," AIAA Paper 85-0360, Jan. 1985.

[9]Degani, D., and Schiff, L. B., "Computation of Turbulent Supersonic Flows Around Pointed Bodies Having Crossflow Separation," *Journal of Computational Physics*, Vol. 66, Sept. 1986, pp. 173–196.

[10]Thomas, J. L., Taylor, S. L., and Anderson, W. K., "Navier-Stokes Computations of Vortical Flows Over Low Aspect Ratio Wings," AIAA Paper 87-0207, Jan. 1987.

[11]Chakravarthy, S. R., Szema, K. Y., and Haney, J. W., "Unified Nose-to-Tail Computational Method for Hypersonic Vehicle Applications," AIAA Paper 88-2564, June 1988.

[12]Baysal, O., Fouladi, K., and Miller, D. S., "Computations of Supersonic Flows Over a Body at High Angles of Attack," *AIAA Journal*, Vol. 27, No. 4, 1989, pp. 427–437.

[13]Thomas, J. L., Walters, R. W., Reu, T., Ghaffini, S., Weston, R. P., and Duckering, J. M., "Patched Grid Algorithm for Complex Configurations Directed Toward F-18 Aircraft," AIAA Paper 89-0121, Jan. 1989.

[14]Baldwin, B. S., and Lomax, H., "Thin Layer Approximation and Algebraic Model for Separated Flows," AIAA Paper 78-257, Jan. 1978.

[15]Van Leer, B., "Flux-Vector Splitting for the Euler Equations," *Lecture Notes in Physics*, Vol. 170, Springer-Verlag, Berlin, 1982, pp. 507–512.

[16]Wardlaw, A. B., Jr., and Davis, S. F., "A Second Order Godunov Method for Supersonic Tactical Missiles," Naval Surface Warfare Center, NSWC TR 86-506, Silver Spring, MD, Dec. 1986.

[17]Keener, E. R., "Oil-Flow Separation Patterns on an Ogive Forebody," NASA TM81314, Oct. 1981.